Measurements and simulations of the near-surface composition of evaporating ethanol–water droplets

Christopher J. Homer,[a] Xingmao Jiang,[b] Timothy L. Ward,[c] C. Jeffrey Brinker[bcd] and Jonathan P. Reid*[a]

Received 26th February 2009, Accepted 7th May 2009
First published as an Advance Article on the web 3rd June 2009
DOI: 10.1039/b904070f

The evolving composition of evaporating ethanol–water droplets (initially 32.6 or 45.3 μm radius) is probed by stimulated Raman scattering over the period 0.2 to 3 ms following droplet generation and with a surrounding nitrogen gas pressure in the range 10 to 100 kPa. The dependence of the evaporation rate on the relative humidity of the surrounding gas phase is also reported. The measured data are compared with both a quasi-steady state model and with numerical simulations of the evaporation process. Results from the numerical simulations are shown to agree closely with the measurements when the stimulated signal is assumed to arise from an outer shell with a probe depth of 2.9 ± 0.4% of the droplet radius, consistent with a previous determination. Further, the time-dependent measurements are shown to be sensitive to the development of concentration gradients within evaporating droplets. This represents the first direct measurement of the spatial gradients in composition that arise during the evaporation of aerosol droplets and allows the influence of liquid phase diffusion within the condensed phase on droplet evaporation to be examined.

I. Introduction

It is important to understand the mass and heat transfer occurring during the growth or evaporation of liquid aerosol droplets when studying the rapid evaporation processes that occur during the delivery of fuels for combustion, the delivery of drugs to the lungs and during spray drying.[1–5] The rapid evaporation of volatile components can lead to substantial changes in droplet surface temperature, thereby influencing the mass transfer rate.[6] Significant gradients in composition can be established in the condensed phase as the droplet evaporates if the rate of liquid phase diffusion is slow compared to the rate of mass transfer to the surrounding vapour.[1] The evaporation dynamics are unsteady and the coupled mass and energy conservation equations must be solved simultaneously.[7–9]

Numerous experimental techniques have been applied to study the rates of mass and heat transfer of growing or evaporating aerosol. Many of the measurements on individual isolated droplets have been made with electrostatic, acoustic or optical traps, and have focused on the determination of component vapour pressures through measurements of the slow evaporation of low volatility organic components.[10–13] The droplet size has been commonly determined by elastic light scattering or evolving mass. Under these conditions, the evaporation process can be assumed to proceed isothermally and the mass and heat transfer can be decoupled. There are few examples of the direct characterisation of the unsteady evaporation of aerosol droplets.[6–9,14] Elastic light scattering has been applied to probe evolving particle size and refractive index. However, there have been very few direct measurements of evolving particle composition.[15–18]

We have shown that the non-linear stimulated Raman signature from evaporating mixed component droplets, referred to below as cavity enhanced Raman scattering (CERS), can be used to characterise the evolving composition of evaporating alcohol/water droplets.[15,16] By combining pulsed laser illumination with a droplet train instrument, the depletion in concentration of the more volatile alcohol component can be determined with variation in surrounding gas pressure over time frames from 0.2 to 10 ms. The amplification of the Raman signal occurs at wavelengths commensurate with whispering gallery modes (WGMs) and the signal intensity from a particular component scales exponentially with concentration. Thus, CERS provides a highly sensitive signature of composition: the composition of ethanol–water solution droplets can be determined with an accuracy of ±0.2% v/v over the compositional range 16 to 19% v/v ethanol in water, where % v/v refers to the percentage by volume of the alcohol prior to mixing, with balance of water. We have used this technique to measure the depletion of methanol, ethanol or propanol from mixed alcohol/water droplets,[15,16] initially in the radius range 20–60 μm, at surrounding dry nitrogen gas pressures in the range 10 to 100 kPa.

In our previous work, the experimental measurements at a fixed and early evaporation time of 0.2 ms were compared to a

[a] *School of Chemistry, University of Bristol, Bristol, UK BS8 1TS*
[b] *Center for Micro-Engineered Materials, University of New Mexico, Albuquerque, NM 87106, USA*
[c] *Departments of Chemical and Nuclear Engineering and Molecular Genetics and Microbiology, University of New Mexico, Albuquerque, NM 87106, USA*
[d] *Sandia National Laboratories, Albuquerque, NM 87106, USA*

quasi-steady model (QSS), initially presented by Newbold and Amundsen.[19] This approach assumes that at any particular instant in time the concentration and temperature profiles in the surrounding gas-phase can be represented by a steady state profile.[20,21] Changes in temperature or concentration profile are accompanied by a change in the boundary conditions at the droplet surface. This is a good approximation if the timescale for adopting a stable temperature and concentration profile in the gas phase is short compared to the timescale over which the boundary conditions are changing.[20]

A major failing of the QSS model used in our previous work is that it does not account for the developing concentration and temperature gradients that are established within the droplet. For example, the initial more rapid loss of the volatile alcohol component than the aqueous component from the droplet surface leads to surface depletion of the alcohol while the droplet bulk remains at the initial composition.[16,22] When accompanied by the temperature depression at the surface, it is anticipated that the mass flux of the alcohol from the surface should decrease over time.[23] Given that the non-linear Raman signal provides a measure of the composition in the outer shell of the droplet, the failure of the QSS model to represent the evaporation dynamics with increasing time or increasing mass flux of alcohol from the droplet is to be expected.

In this publication we present new measurements of the evolving composition of ethanol–water droplets, extending our previous measurements to times longer than 0.2 ms and up to 3 ms over a range of gas pressures from 10 to 100 kPa. The failure of the QSS model to represent the evaporation process is illustrated over this extended range of conditions. A numerical simulation of droplet evaporation is presented and compared to the experimental observations, demonstrating that the measurements are able to characterise the developing concentration gradients near the droplet surface during evaporation.

II. Theoretical representations of droplet evaporation

Two models have been used to simulate the experimental measurements of the depletion of ethanol with change in gas pressure and with evolving time. The first model is the QSS model, initially presented by Newbold and Amundsen.[19] This has been discussed at length in previous publications.[16,23] The second method, based on numerical simulation, is discussed in this publication.

II.a The quasi-steady state model

In previous publications, we have used the QSS model to simulate the composition and temperature of binary droplets containing alcohol and water of different initial radii at an evaporation time of 0.2 ms and at surrounding gas pressures in the range 10–100 kPa.[16,23] Systems studied have included the evaporation of binary droplets of methanol–water, ethanol–water and 1-propanol/water, and the ternary system methanol–ethanol/water.[16,22,23]

A number of assumptions are inherent to the QSS treatment.[16,19] Firstly, the composition of the gas phase at the liquid surface is assumed to be governed by equilibrium thermodynamics, with a composition determined by the liquid phase composition and temperature at the surface. The effect of surface tension on vapour pressure is assumed to be negligible and is ignored. Further, the profiles of temperature and composition surrounding the droplet can be approximated to steady-state profiles at any instant in time. Finally, it is assumed that mass and heat transfer within the droplet are instantaneous compared to transfer within the gas phase and, as a consequence, the temperature and composition remain uniform throughout the entire droplet volume.

The assumption of spatial uniformity in composition during evaporation must be contrasted with the origin of the CERS signal, which is sensitive only to the composition near the droplet surface, rather than the whole droplet bulk. Thus, the CERS signal is expected to provide a measure of the alcohol depletion in the outer shell of the droplet to a maximum probe depth of $\sim$25% of the droplet radius.[24] Indeed, our previous work has suggested that the signal arises from a much narrower volume element with shorter penetration depth from the surface: the signal is non-linear and double resonance in origin and, thus, more spatially confined than the penetration depth of WGMs.[16] A schematic of the droplet highlighting these different regions is presented in Fig. 1a.

To account for the near-surface sensitivity of the CERS measurement, it was shown that a constant scaling of the QSS bulk average depletion could be used to adequately represent the experimentally determined trends for a broad range of initial droplet radii and gas pressures at an early evaporation time.[16] Indeed, it was shown that a constant scaling factor of

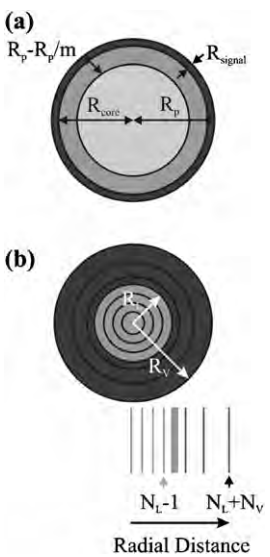

Fig. 1 (a) R_{signal}, R_{core} and R_p are defined as: the estimated thickness of the outer shell from which the signal originates, the radius of the core that is not interrogated by the Raman signal and the particle radius, respectively. The estimated penetration depth of WGMs is also indicated. (b) The radial distribution of shells used in the numerical simulation is shown for the liquid droplet (light grey) and surrounding gas phase (dark grey). The droplet of radius R_p is divided into N_L concentric control elements of equal thickness. The gas phase is separated into N_V concentric layers of increasing thickness for efficient simulation.

11.4 ± 3.0 could be used to represent all of the binary systems studied, methanol–water, ethanol–water and 1-propanol–water, at an evaporation time of 0.2 ms. This scaling factor was shown to be equivalent to assuming that the probe depth of the CERS signal was only $\sim$3% of the droplet radius, typically 1 μm for the droplet sizes studied.

The use of a single scaling factor to represent all of the alcohol/water systems studied by the QSS model can be attributed to two key factors. Firstly, the refractive indices of all binary and ternary solutions studied are similar, with the consequence that the optical probe depth is expected to be similar for all three systems.[16,25] Secondly, the liquid phase diffusion coefficients for all alcohol components are similar in magnitude. When considered in conjunction with the early evaporation times studied ($\sim$0.2 ms for all systems), the gradient in composition arising from surface depletion is expected to be established over a much shorter length scale than the probe depth. Thus, it is anticipated that the QSS representation of the experimental data should deteriorate at longer fall times, higher depletions of alcohol and for smaller droplets, and that the required scaling factor is not a constant. This is in addition to the clear failings of the QSS model to reflect the details of the dynamic processes occurring.

II.b Numerical simulation of the moving boundary problem

A second, more appropriate numerical simulation is now presented as an alternative to the QSS model to simulate the evaporation of binary alcohol/water droplets.[26] The physical properties of an evaporating droplet are interconnected and change nonlinearly with time. The droplet boundary is also changing with time as the droplet grows or evaporates. This leads to a one-dimensional time-dependent moving boundary Stefan problem. Mathematical analysis of this moving boundary problem is complex, and much research has been conducted to find a solution to this problem. Fixed[27] and variable[28–30] time-step methods have been developed to examine the problem with implicit boundary conditions; these methods are discussed and compared in detail by Moyano and Scarpettini.[31] Further attempts to solve the problem have also been proposed by Rizwan-Uddin,[32] Asaithambi[33] and Caldwell *et al.*[34]

The numerical simulation presented here circumvents the difficulty of solving the moving boundary problem by converting it to a fixed boundary problem by assuming that the boundary does not move over a small time step. A full description of the simulation method will be presented by Jiang and Brinker in a subsequent paper and details are presented in ref. 26. The purpose of this publication is to compare the numerical simulations with the experimental data and only a brief description of the model will be presented here.

The droplet and its surrounding vapour phase are divided into a large number of concentric segments (Fig. 1b), respectively N_L and N_V. For computational efficiency, the initial volume elements are designed with varying size and are chosen to be most dense for the regions near the droplet surface where gradients in concentration and temperature are steep. The control volumes near the surface may be merged with a neighbouring layer of the same phase or divided into two layers to keep the grid spacing small and enable convergence, accuracy and quick numerical simulation. For modelling the evaporation of a droplet into an 'infinite' volume of air, the vapour phase grid spacings are chosen to take a power relationship to reduce N_V and increase the efficiency of simulation without compromising the accuracy. The Stefan problem is then treated as an integration of a series of small consecutive changes as the physical properties of the droplet change with time, $t \rightarrow t + \delta t$. This allows the calculation of mass and heat transfer for a droplet with a fixed boundary; the new boundary is determined after each time step and the calculation repeated. When performed with a series of small time steps and with a small enough grid size, the calculations approximate closely to the solution that would be achieved if the problem were treated as a moving boundary problem.

More specifically, the evaporation dynamics characterised in the experiments can be treated within the continuum regime and are controlled by gas phase diffusion. As in the QSS model, the vapour and liquid phases at the droplet surface are assumed to remain at equilibrium. For a spherical stationary system without chemical reaction, the mass transport of this isotropic diffusion system can be described by a continuity equation for species i:

$$\frac{\partial C_i}{\partial t} = \frac{1}{r^2}\frac{\partial}{\partial r}\left(r^2 D_i \frac{\partial C_i}{\partial r}\right) \quad (1)$$

where C_i is the concentration of component i, t is the evaporation time, D_i is the diffusion coefficient of component i and r is the radial distance. Similarly, the heat transport can be described as

$$\frac{\rho C_P \partial T}{\partial t} = \frac{1}{r^2}\frac{\partial}{\partial r}\left(r^2 k \frac{\partial T}{\partial r}\right) \quad (2)$$

where ρ is the density of the solution or gas phase, C_P is heat capacity of the solution or gas phase and T is the temperature. Eqn (1) and (2) are valid only for evaporation without radial convection. This is a reasonable approximation for droplets with negligible internal pressure gradient and for which concentration and temperature gradients result in mass and thermal diffusion alone. These partial differential equations are difficult to solve simultaneously as all physical properties are interconnected and change with time and location. In addition, the droplet size changes with time.

To solve the coupled mass and heat transport problem, the moving boundary problem can be solved explicitly as an integration of a series of consecutive conventional fixed-boundary heat-transport-only, mass-transport-only, and control volume shrinkage/expansion-only steps.[26] The time step can be fixed at a low value (10^{-6} s) or increased gradually with developing temperature and concentration profiles to reduce computational time while ensuring convergence of the simulation.[26] Eqn (1) and (2) are solved by a finite difference method subject to the following initial and boundary conditions. Considering an initial concentration distribution that is uniform throughout the droplet,

the initial and boundary conditions for component i are given as follows:

$$C_i(r,0) = C_{i,0} \text{ for } 0 \le r \le R_{\mathrm{NL},0} \quad (3)$$

$$C_i(r,0) = C_{i,0,\mathrm{V}} \text{ for } R_{\mathrm{NL},0} < r \le R_{\mathrm{NL+NV},0} \quad (4)$$

$$\left(\frac{\partial C_i}{\partial r}\right)\Big|_{r=0} = 0 \quad (5)$$

$$\left(\frac{\partial C_i}{\partial r}\right)\Big|_{R_{\mathrm{NL+NV}}} = 0 \text{ or } C_i = C_{i,\infty} \text{ at } R_{\mathrm{NL+NV}} = \infty \quad (6)$$

R_{NL} and $R_{\mathrm{NL+NV}}$ are droplet radius and the radius of outermost vapor layer. A subscript of 0 denotes $t = 0$ s, or the initial state. The mass balance for component i in the liquid layer (NL) at the interface during time t and $t + \delta t$ can be written as:

$$\begin{aligned} &R_{\mathrm{NL}-1}^2(R_{\mathrm{NL}} - R_{\mathrm{NL}-1})\frac{C_{i,\mathrm{NL}}(t+\delta t) - C_{i,\mathrm{NL}}(t)}{\delta t} \\ &= 2R_{\mathrm{NL}}^2 D_{i,\mathrm{NL}}^{\mathrm{V}} \frac{C_{i,\mathrm{NL}+1}(t) - C_{i,\mathrm{NL,eq}}(t)}{R_{\mathrm{NL}+1} - R_{\mathrm{NL}}} \\ &\quad - R_{\mathrm{NL}-1}^2 D_{i,\mathrm{NL}-1}\frac{C_{i,\mathrm{NL}}(t) - C_{i,\mathrm{NL}-1}(t)}{R_{\mathrm{NL}} - R_{\mathrm{NL}-1}} \end{aligned} \quad (7)$$

where the $D_{i,\mathrm{NL}}^{\mathrm{V}}$ refers to the diffusion coefficient of i in the first vapour layer, and $C_{i,\mathrm{NL,eq}}$ is the vapor phase concentration at equilibrium with liquid compositions for the liquid layer, NL. For the first vapour element, the mass balance is:

$$\begin{aligned} &R_{\mathrm{NL}}^2(R_{\mathrm{NL}+1} - R_{\mathrm{NL}})\frac{C_{i,\mathrm{NL}+1}(t+\delta t) - C_{i,\mathrm{NL}+1}(t)}{\delta t} \\ &= R_{\mathrm{NL}+1}^2 D_{i,\mathrm{NL}+1}\frac{C_{i,\mathrm{NL}+2}(t) - C_{i,\mathrm{NL}+1}(t)}{R_{\mathrm{NL}+2} - R_{\mathrm{NL}+1}} \\ &\quad - 2R_{\mathrm{NL}}^2 D_{i,\mathrm{NL}}^{\mathrm{V}}\frac{C_{i,\mathrm{NL}+1}(t) - C_{i,\mathrm{NL,eq}}(t)}{R_{\mathrm{NL}+1} - R_{\mathrm{NL}}} \end{aligned} \quad (8)$$

Correspondingly, the initial and boundary conditions for heat transport can be defined in a similar way as:

$$T(r,0) = T_{0,L} \text{ for } 0 \le r \le R_{\mathrm{NL},0} \quad (9)$$

$$T(r,0) = T_{0,V} \text{ for } R_{\mathrm{NL},0} < r \le R_{\mathrm{NL+NV},0} \quad (10)$$

$$\left(\frac{\partial T}{\partial r}\right)\Big|_{r=0} = 0 \quad (11)$$

$$\left(\frac{\partial T}{\partial r}\right)\Big|_{R_{\mathrm{NL+NV}}} = 0 \text{ or } T = T_\infty \text{ at } R_{\mathrm{NL+NV}} = \infty \quad (12)$$

The heat balance for the outer liquid layer (NL) can be written as the following equation:

$$\begin{aligned} &R_{\mathrm{NL}-1}^2(R_{\mathrm{NL}} - R_{\mathrm{NL}-1})\rho_{\mathrm{NL}}C_{\mathrm{PNL}}\frac{T_{\mathrm{NL}}(t+\delta t) - T_{\mathrm{NL}}(t)}{\delta t} \\ &= 2R_{\mathrm{NL}}^2 k_{\mathrm{NL}}^{\mathrm{V}}\frac{T_{\mathrm{NL}+1}(t) - T_{\mathrm{NL}}(t)}{R_{\mathrm{NL}+1} - R_{\mathrm{NL}}} \\ &\quad + 2R_{\mathrm{NL}}^2\sum_i D_{i,\mathrm{NL}}^{\mathrm{V}}\frac{C_{i,\mathrm{NL}+1}(t) - C_{i,\mathrm{NL,eq}}(t)}{R_{\mathrm{NL}+1} - R_{\mathrm{NL}}}\Delta\bar{H}_{i,evp} \\ &\quad - R_{\mathrm{NL}-1}^2 k_{\mathrm{NL}-1}\frac{T_{\mathrm{NL}}(t) - T_{\mathrm{NL}-1}(t)}{R_{\mathrm{NL}} - R_{\mathrm{NL}-1}} \end{aligned} \quad (13)$$

and for the first vapor element as:

$$\begin{aligned} &R_{\mathrm{NL}}^2(R_{\mathrm{NL}+1} - R_{\mathrm{NL}})\rho_{\mathrm{NL}+1}C_{\mathrm{PNL}+1}\frac{T_{\mathrm{NL}+1}(t+\delta t) - T_{\mathrm{NL}+1}(t)}{\delta t} \\ &= R_{\mathrm{NL}+1}^2 k_{\mathrm{NL}+1}\frac{T_{\mathrm{NL}+2}(t) - T_{\mathrm{NL}+1}(t)}{R_{\mathrm{NL}+2} - R_{\mathrm{NL}+1}} \\ &\quad - 2R_{\mathrm{NL}}^2 k_{\mathrm{NL}}^{\mathrm{V}}\frac{T_{\mathrm{NL}+1}(t) - T_{\mathrm{NL}}(t)}{R_{\mathrm{NL}+1} - R_{\mathrm{NL}}} \end{aligned} \quad (14)$$

where k is heat conduction coefficient and $\Delta\bar{H}_i$ is the partial molar evaporation heat for component i. The solubility of air or nitrogen in the droplets is neglected.

Adjustment of the control volumes is achieved by self-attuning based on mass balance and pressure conservation following the updated temperature and concentrations. Primed and unprimed quantities refer to the property after or before the time increment, respectively. The volume shrinkage/expansion coefficient, η_j^{L} for liquid layer j over time δt can be obtained by

$$\eta_j^{\mathrm{L}} = \frac{V_j'}{V_j} = \frac{\frac{4}{3}\pi(R_j'^3 - R_{j-1}'^3)}{\frac{4}{3}\pi(R_j^3 - R_{j-1}^3)} = \frac{\sum_i mw_i C_i'}{\sum_i mw_i C_i}\cdot\frac{\rho}{\rho'} \quad (15)$$

where ρ is a function of composition and temperature, mw_i is the molecular weight for component i, and C'_i, R'_i, and ρ' are the updated concentration for component i at the updated radius and updated density for jth element. Similarly, the volume shrinkage/expansion coefficient, η_j^L for vapor layer j over time δt is given by

$$\eta_j^V = \frac{V_j'}{V_j} = \frac{\sum_i mw_i C_i'}{\sum_i mw_i C_i}\cdot\frac{\overline{mw}}{\overline{mw'}}\cdot\frac{T'}{T} \quad (16)$$

Where T and T' are the temperatures, and $\overline{mw}$ and $\overline{mw'}$ are the average molecular weight at t and $t + \delta t$ for the jth vapour layer. The volume updating starts first from the element at droplet center and gradually extends outward to the liquid layer near droplet interface and then to vapor layers while keeping a fixed total gas pressure.

The initial conditions are used to update C and T and, therefore, all other transient thermodynamic and transport properties by mass balance (eqn (1)) and thermal balance (eqn (2)) for each layer (element, control volume) within the vapour phase and liquid phase over a time period $t = 0 \rightarrow \delta t$. The boundary conditions are coupled to the updating of the properties for the liquid layer at the droplet centre and at the outermost vapour layer throughout all the simulation. Step-by-step, all thermodynamic and transport properties for each element can be calculated and updated over the evaporation time. A discussion of the methods for describing the solution thermodynamics and the thermophysical properties required for these simulations is presented in Appendix A.

II.c Numerical simulations of internal gradients in composition

With the QSS model, the total ethanol depletion is estimated from the whole of the droplet volume; there is no

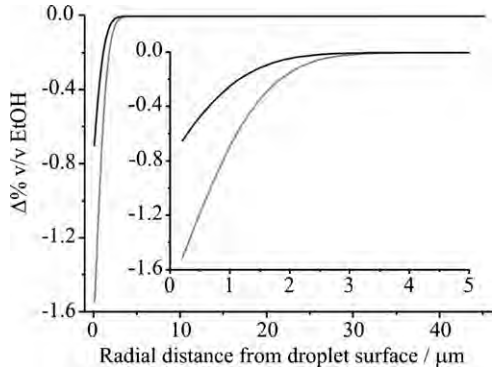

Fig. 2 The radial dependence of the ethanol concentration within a droplet, initially 45.3 μm in radius, probed at an evaporation time of 0.5 ms. The composition of the droplet is initially 18.4% v/v ethanol, balance water. The grey line represents calculations at a chamber pressure of 10 kPa and the black line represents a chamber pressure of 100 kPa. The inset figure shows a more detailed view of the change in ethanol depletion in the outer 5 μm shell of the droplet.

consideration of the developing spatial inhomogeneities in composition at different radial depths within the droplet. In contrast, the numerical simulations explicitly include information on the heat and mass transfer occurring with the condensed phase by resolving the droplet into a number of concentric layers. Thus, the ethanol depletion in each layer can be estimated, providing a radial profile of ethanol concentration throughout the droplet volume and allowing treatment of the heat and mass transfer occurring in both the liquid and gas phases.

Fig. 2 illustrates the simulated radial concentration profile of a single isolated droplet, initially 45.3 μm in radius and with a composition of 18.4% v/v ethanol, resolved into 452 layers of ~100 nm thickness at an evaporation time of 0.5 ms. Greater depletion occurs near the surface of the droplet, establishing a concentration gradient that drives diffusion of ethanol within the droplet from the bulk towards the surface. The higher evaporative mass flux of ethanol from the droplet at lower pressures (compare 100 and 10 kPa in Fig. 2) leads to a more significant depletion of ethanol at the surface and a larger concentration gradient within the droplet.

Fig. 3 presents the temporal evolution of the ethanol depletion calculated at various depths from the droplet surface at surrounding gas pressures in the experimental chamber of 10 kPa and 100 kPa. It can be seen that depletion is greater at a fixed depth within the droplet when the surrounding gas pressure is lower. Further, although ethanol is depleted in concentration within the CERS probe volume (*e.g.* 250 nm) from the very early times, the slow rate of liquid diffusion ensures that the core of the droplet does not change in composition until considerably later in time (*e.g.* compare depths of 1 μm and 10 μm). This is the origin of the scaling factor that must be introduced to allow comparison of the estimated depletions from the QSS model and the experimental measurements. Indeed, after ~2 ms, the concentration of ethanol at a depth of 250 nm begins to recover as liquid diffusion replenishes the level of ethanol near the droplet surface.

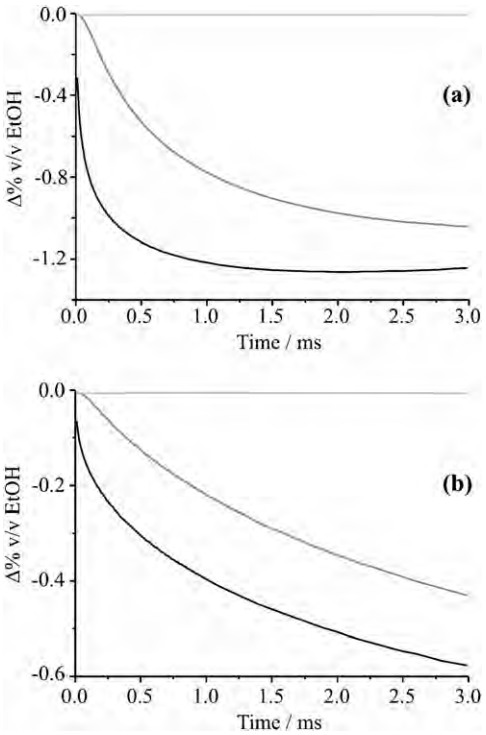

Fig. 3 The ethanol depletion predicted by the numerical simulations at depths of 250 nm (black lines), 1 μm (grey lines) and 10 μm (light grey lines) in a single stationary droplet of 45.3 μm radius: (a) A chamber pressure of 10 kPa; (b) a chamber pressure of 100 kPa.

Fig. 4 shows the radial profile of ethanol, water and nitrogen mole fractions in the gas phase at a variety of fall times. As expected, the gaseous mole fractions of ethanol and water decrease as the distance from the droplet surface increases with a range of order ~20 μm after ~2 ms. The gas phase is enriched in ethanol compared to the solution surface, in accordance with the positive deviation of the ethanol vapour pressure from Raoult's law for this solution composition.[35]

The QSS model and numerical simulation consider heat and mass transfer from a single, isolated droplet. However, the experiment uses a vibrating orifice aerosol generator to produce a train of falling droplets. The motion of the particles and their close proximity to one another must be taken into account in the simulations.[14] As the particles are moving, convection is occurring as well as conduction, and so the mass transfer from the droplet will be enhanced.[36] The proximity of the falling droplets also suggests that it is possible that the evaporated gas from one droplet may impact the evaporation rate of subsequent droplets falling through the vapour field.

II.d Corrections for droplet motion and for the interference between successive droplets in the droplet train

The influence of the motion of the droplets on the evaporation rate can be estimated by including a scaling of the mass flux within a time interval by the Sherwood number, Sh.[6] For diffusion from a stationary droplet, Sh = 2. However, when a

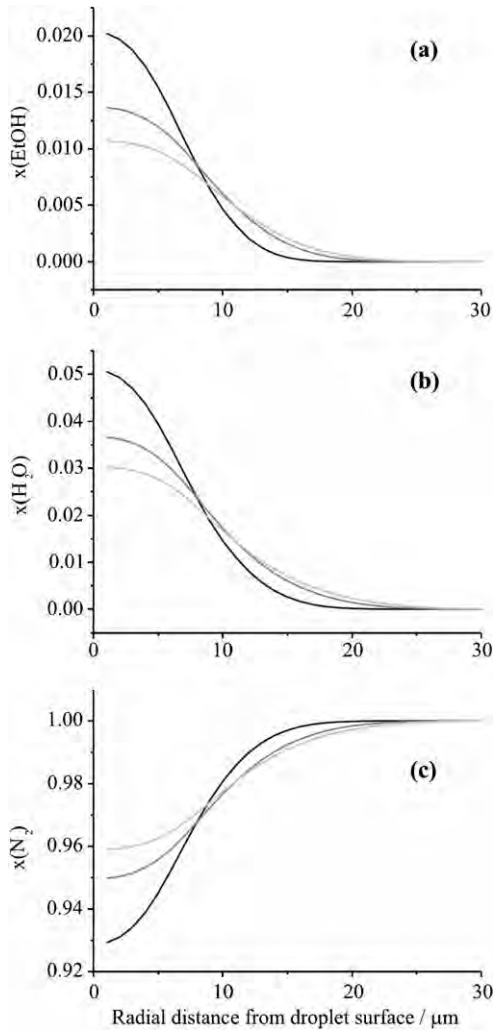

Fig. 4 The radial profile of the gas phase surrounding the droplet, showing the mole fractions of ethanol (a), water (b) and nitrogen (c) as the distance from the droplet surface varies. These simulations were calculated for a 45.3 μm radius droplet evaporating at a chamber pressure of 100 kPa and fall times of 0.5 ms (black lines), 1.5 ms (grey lines) and 2.5 ms (light grey lines).

droplet is falling, the evaporation rate can be enhanced and the value of Sh can be calculated from:

$$\mathrm{Sh} = 2 + 0.6\sqrt{\mathrm{Re}}\sqrt[3]{\mathrm{Sc}} \qquad (17)$$

Re and Sc are respectively the Reynolds and Schmidt numbers, calculated from:

$$\mathrm{Re} = \frac{v_t 2R_p}{v_{air}} \qquad (18)$$

$$\mathrm{Sc} = \frac{v_{air}}{D_g} \qquad (19)$$

v_t and v_{air} are the terminal velocity of the droplet and the kinematic viscosity of air respectively.

Chen *et al.*[37] and Devarakonda and Ray[14] considered the change in evaporation rate when evaporation is from a train of closely spaced droplets rather than an isolated droplet. Devarakonda and Ray[14] showed that an empirical correction, referred to as the inter-particle interaction parameter, η, could be used to effectively scale and account for the mass flux from the droplet in a specified time interval.

$$\eta = 0.0611 + 0.0505\left(\frac{l}{R_p}\right) + 0.0029\left(\frac{l}{R_p}\right)^2 \qquad (20)$$

l is the distance between droplet centres. In this work, we limit our discussion to the inclusion of this empirical scaling, rather than attempting to model the coupling in greater detail.

The experimental data presented in this publication were obtained from droplets with a Sherwood number in the range 5.9–6.7 and the interaction parameter in the range 0.69–0.81. An appropriate scaling to correct for both of these factors is included in all of the theoretical simulations presented here in a manner identical to our previous work.[16]

III. Experimental

The experimental apparatus used to conduct this research has been described in detail elsewhere, and only a brief overview will be given here.[15,38] A monodisperse train of droplets is produced using a vibrating orifice aerosol generator (VOAG).[39] To produce this train, the binary ethanol–water solution is forced through an orifice disc of 25 or 35 μm in diameter. A square wave of amplitude 0–10 V and frequency 20–70 kHz drives the piezoelectric crystal inside the VOAG, breaking the liquid jet into droplets. Droplets of radii 27.3–51.8 μm with a Gaussian size distribution of 4 ± 200 nm and a fall speed of 12.14 ± 0.1 ms^{-1} can be generated. The third harmonic (355 nm) of a Nd:YAG laser is used as the excitation source for the Raman measurements and is focused to illuminate a single droplet from the train with a pulse energy of ~0.2–0.5 mJ pulse^{-1}.

The droplet train falls within a custom-fabricated chamber allowing control of the gas phase environment. A detailed description of this chamber can be found elsewhere.[38] Dry nitrogen flows through the chamber at a rate of 5 L min^{-1}. For the experiments conducted under increased relative humidity, a flow of water vapour is required. To achieve this, two bubblers containing distilled water are set up in series, and nitrogen gas bubbled through them. The resultant flow is mixed with dry nitrogen prior to entering the chamber. The flow rate of the humidified nitrogen gas is varied between 1–5 L min^{-1}; the total flow rate of gas entering the chamber is kept constant at 5 L min^{-1} by altering the flow rate of dry nitrogen gas.

Raman scattered light is collected perpendicular to the incident beam in the horizontal plane. The Raman scattered light from the chamber is collimated and focused through the entrance slit of a 0.5 m spectrograph. The light is dispersed onto an intensified CCD detector consisting of 256 rows of 1024 pixels. A diffraction grating of 2400 grooves mm^{-1} is used to collect the spectra, giving a spectral dispersion of 0.012 nm pixel^{-1}. Spectra are collected from 2500 different droplets as they fall through the probe region, and a cumulative spectrum analysed for each set of results. The composition of the droplets is determined using the procedure

to analyse the non-linear Raman signature established in previous work.[15,16,40]

IV. Results and discussion

The depletion of ethanol has been measured for binary ethanol–water droplets of initial radii of 32.6 and 45.3 μm and composition 18.4% v/v ethanol at evaporation/fall times between 0.3 and 3 ms and dry nitrogen gas pressures between 10 and 100 kPa. In these measurements it is essential to remember that the signal arises from the outer shell of the droplet, rather than the droplet bulk, providing a measure of the near surface composition and depletion of ethanol. Initially, ethanol evaporates more rapidly from the droplet giving rise to a concentration gradient within the droplet. The concentration gradient is accompanied by liquid diffusion which acts to counteract the initial depletion of ethanol. In addition, the cooling of the surface leads to unsteady evaporation and a relative change in mass flux of the two components. Thus, it is essential to consider the depth probed by the Raman signal and how an appropriate average value can be estimated from the spatially resolved numerically simulated depletions for comparison to the experimental observations.

IV.a Consideration of the probe depth

In order to obtain a spatially averaged value for the ethanol depletion for comparison with the experiments, it is necessary to take into account the compositional variation over the depth to which the droplet is being probed and the radial distribution of the light intensity[41] circulating within WGMs inside the droplet. More specifically, the calculated mole fraction of ethanol in each shell, $x_{d,\mathrm{EtOH}}$, at a distance from the centre of the droplet, d, must be weighted by a scaling factor, $W_{\mathrm{G},d}$.

$$x_{v,\mathrm{EtOH}} = x_{d,\mathrm{EtOH}} \times W_{\mathrm{G},d} \tag{21}$$

The weightings of each shell volume are assumed to follow a Gaussian distribution around a dominant shell that is set to have the maximum weighting, the shell that is considered to contain the highest light intensity. This is subsequently referred to as the probe depth, although it should be remembered that this only represents the shell with the maximum weighting and light does penetrate to a greater depth. The weight for each volume element is calculated from

$$W_{\mathrm{G},d} = \frac{1}{\sigma\sqrt{2\pi}} e^{-(V_{\mathrm{layer}}-\mu)^2/2\sigma^2} \tag{22}$$

where μ is the value of the volume element at the maximum intensity of the Gaussian intensity distribution and σ is chosen such that the integrated intensity of the Gaussian weighting distribution remains independent of the chosen probe depth and is equal to unity. Further, the Gaussian weighting is chosen such that it decays to $<5\%$ of the peak, effectively zero weighting, at the boundary of the droplet. Thus, the maximum amplitude of the Gaussian weighting function decreases as deeper regions of the droplet are allowed to contribute to the signal and the radial range of the weighting extends further from the droplet surface. Although the light intensity distribution circulating within the droplet is not accurately known, it is considered that a Gaussian weighting should best represent the origin of the CERS double resonance signal.[24,41]

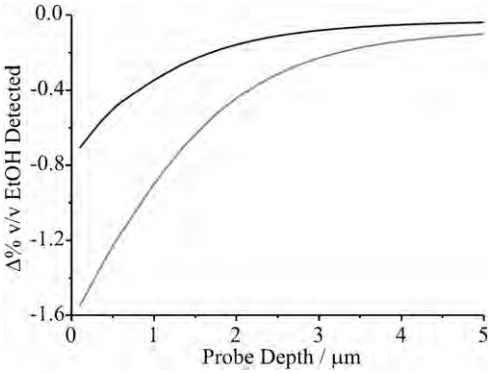

Fig. 5 The simulated ethanol depletion that would be detected with varying laser probe depth for a 45.3 μm radius droplet at an evaporation time of 0.5 ms and chamber pressures of 10 kPa (grey line) and 100 kPa (black line).

The volume element, V_{layer}, of each concentric shell is approximated by

$$V_{\mathrm{layer}} = 4\pi R_{\mathrm{inner}}^2 \cdot \mathrm{d}R \tag{23}$$

where $\mathrm{d}R$ is the thickness of the shell and R_{inner} is the inner radial coordinate at which the shell is located. To obtain the weighted mole fraction of ethanol across the entire probe volume, the sum of $x_{v,\mathrm{EtOH}}$ is divided by the sum of the Gaussian weighting elements.

$$x_{\mathrm{EtOH}} = \frac{\sum x_{v,\mathrm{EtOH}}}{\sum W_{\mathrm{G},d}} \tag{24}$$

Fig. 5 shows the prediction of the ethanol depletion that would be recorded from the Raman measurement as the probe depth of the laser is allowed to vary for a droplet, initially 45.3 μm in radius and with a composition 18.4% per vol ethanol, at an evaporation time of 0.5 ms and at a pressure of 10 kPa or 100 kPa. As the signal is allowed to originate from deeper into the droplet, the depletion of ethanol that would be recorded diminishes due to the spatial inhomogeneity in composition that is established during evaporation.

IV.b Comparison with measurements of depletions at varying gas pressure

Previous work using the experimental technique described here has focused on probing droplets shortly after their production, principally at an evaporation time of 0.2 ms.[15,16] Emphasis was particularly placed on exploring the evaporation rates of different droplet sizes and different volatile components at a range of pressures. Little work has been done to probe the evaporation of droplets on longer timescales, or to assess the accuracy of the QSS model to represent depletion at longer fall times. This paper will compare the numerical simulation and QSS model with experimental measurements of binary ethanol–water droplet evaporation on timescales up to 3 ms.

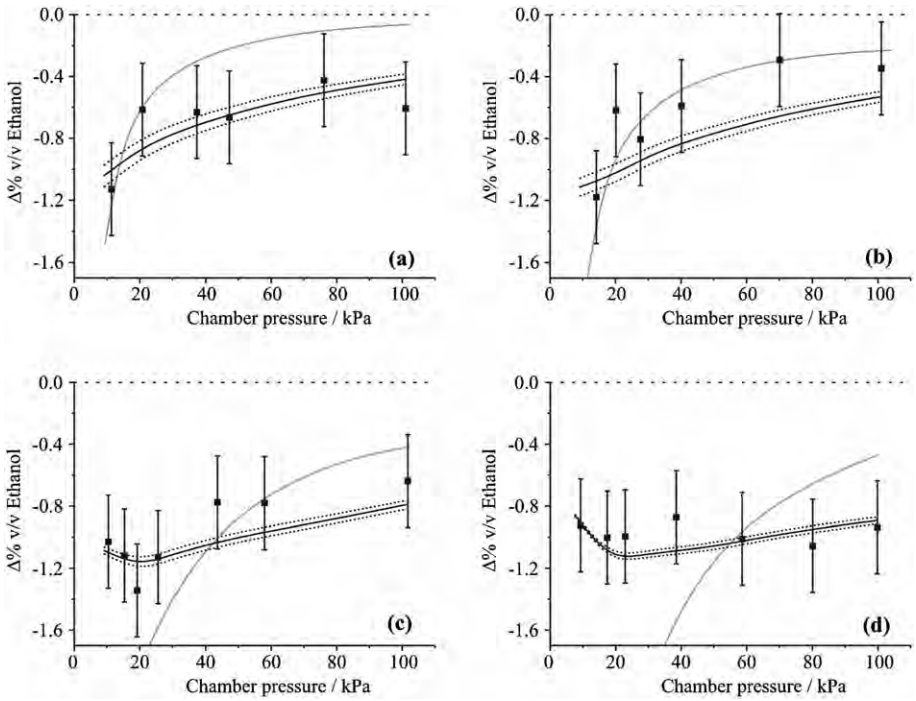

Fig. 6 Pressure dependent evaporation curves which show the ethanol depletion from a 32.6 μm radius droplet at evaporation times of: (a) 0.3 ms, (b) 0.5 ms, (c) 1.3 ms and (d) 2.1 ms. The solid black line represents the numerical simulation for a probe depth of 900 nm and the black dashed lines represent probe depths of 800 and 1000 nm. The solid grey line represents predictions from the QSS model.

In Fig. 6, we report measurements of the depletion of ethanol from evaporating droplets as a function of the surrounding gas pressure and at four evaporation times between 0.3 and 2.1 ms. The droplets are initially 32.6 μm in radius and start with a composition of 18.4% v/v ethanol. The depletion of ethanol at the earliest two fall times increases with decreasing pressure due to the enhanced mass flux of ethanol from the droplet due to the increasing rate of gas diffusion. This is consistent with the trends observed in our previous papers.[15,16] At the longest evaporation time of 2.1 ms the depletion of ethanol does not show a dependence on gas pressure within the error bars of the measurements. Indeed, although the depletion of ethanol decreases steadily at the high pressure limit over the four times shown, the depletion at 10 kPa appears to be less at the longest evaporation time than at 100 kPa. This observation is more obvious when the time dependence is considered explicitly, as shown in Fig. 7(a) and (b). As anticipated in our earlier discussion of the QSS model, the agreement between the QSS predictions and the experimental data is poor, particularly at the longest fall time, predicting greater ethanol depletion than is observed. In this comparison, we have applied the scaling factor of 11.4 determined previously.[15,16]

The results of numerical simulations are also included in Fig. 6 with predictions from probe depths centred around 0.9 μm shown. By considering the quality of the fit to all of the experimental data, this probe depth provides the most accurate description of the data. Not only is the depletion captured at high pressures, but the apparent decrease in the extent of the depletion at the lowest pressures and longest fall times is predicted. Indeed, when compared with the QSS model, the numerical simulations more accurately reflect the time dependence of the depletion, even out to >2 ms, as shown in Fig. 7. The sensitivity of the modelled depletion to the probe depth is apparent from considering the predictions from probe depths of 800 nm and 1000 nm. A probe depth of 900 $\pm$ 100 nm corresponds to the signal originating from a depth between 2.4 and 3.1% of the droplet radius (32.6 μm).

The evaporation of a droplet of initial radius 45.3 μm and composition of 18.4% v/v ethanol has also been studied. Fig. 8 shows the pressure-dependent ethanol depletion measured at evaporation times of 0.5, 0.6, 1.3, 2.1 and 3.0 ms. The QSS model again predicts accurately the ethanol depletion on sub-millisecond timescales, but is not successful in even qualitatively capturing the trend recorded at evaporation times of 1.3 ms and longer. Again, the data shows that the ethanol depletion at early times and low pressures is marked, but this does not continue as time progresses. Instead, the pressure dependence becomes less pronounced and the time dependence shows that the ethanol concentration appears to recover with increasing time (Fig. 7(c)). The numerical simulations again successfully capture the experimental trends for all times and chamber pressures. Simulations from probe depths of 1300, 1400 and 1500 nm are shown for comparison. This is equivalent the signal arising from a probe depth between 2.9 and 3.3% of the initial droplet radius. Thus, the estimated probe depths from both droplet sizes are consistent and equivalent to 2.9 $\pm$ 0.4% of the droplet radius. This is consistent with our previous estimate of the probe depth (3 $\pm$ 1%) based on a comparison of the experimental data with the QSS model but only at the earliest evaporation times.[16]

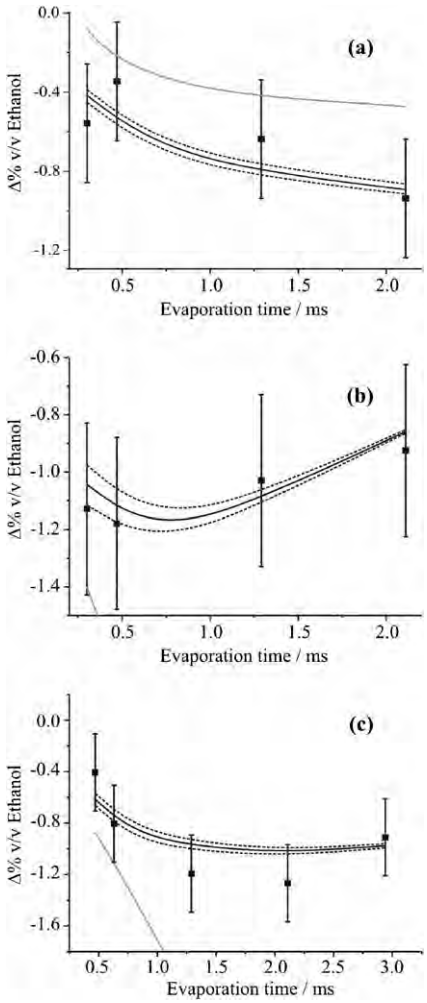

Fig. 7 Comparison of the experimental trends (symbols) and theoretical predictions (QSS model, grey line; numerical simulations, black lines) for the time dependence of the evaporation of (a) 32.6 μm radius droplet at 100 kPa pressure; (b) 32.6 μm radius droplet at 10 kPa pressure; (c) 45.3 μm radius droplet at 10 kPa pressure. The three numerical simulations are for the probe depths reported in Fig. 6 and 8.

IV.c Evaporation measurements at varying relative humidity

The time-dependent ethanol concentration profile has been simulated for a 45.3 μm droplet with varying relative humidity of the gas phase varies. The saturation vapour pressure of water calculated by the model has been altered to take into account the addition of 0.52 and 1.1 kPa of water vapour to the chamber, equivalent to relative humidities of 22 and 47%, respectively, at 20 °C. This diminishes the vapour phase concentration gradient of water between the droplet surface and the infinite distance limit from the droplet, slowing the mass flux of water. Fig. 9(a) shows the effect this has on the predicted ethanol depletion throughout the droplet volume. Increasing the relative humidity of the gas surrounding the droplet increases the modelled ethanol depletion.

In experiments to compare with these predictions, nitrogen gas was passed through two bubblers containing water before being mixed with a dry nitrogen gas flow and then introduced to the aerosol chamber. To measure the dependence of the depletion on gas pressure, the mixing of dry and wet nitrogen was controlled to maintain a constant partial pressure of water in the chamber while changing the overall pressure. In Fig. 9(b), the simulated and measured trends with varying gas pressure and partial pressure of water are compared. It can be seen that the numerical simulations predict, within the experimental error, the extent to which ethanol depletion increases when the relative humidity within the chamber is increased.

V. Conclusions

The QSS model and the numerical simulations have been used to model the evaporation of a binary ethanol–water droplet on timescales up to 3 ms and the predictions are compared with experimental measurements. The QSS model has been shown to be only suitable for considering relative trends in the change in concentration at a fixed evaporation time, requiring a constant scaling factor to account for the spatial variation and gradients in the droplet composition not accounted for by the model.[16] The QSS model fails to accurately capture the experimental trends when the ethanol depletion is large at millisecond and longer evaporation times or when the pressure of the gas surrounding the droplet decreases. Forced agreement between the QSS model and experiment would require the introduction of a time dependent scaling factor, which would indirectly account for the internal dynamics occurring within the condensed phase but would hide the details of the evaporation mechanism.

By contrast, the experimental measurements are found to be consistent with the numerical simulations for all measurements reported in this publication when the probe depth of the stimulated Raman scattering signal is taken as $2.9 \pm 0.4\%$ of the droplet radius. This confirms that the experimental measurements interrogate the spatial inhomogenieties in composition that arise during evaporation. Specifically, the outer shell of the droplet first exhibits a significant depletion in the more volatile alcohol component, followed by a recovery due to liquid phase diffusion; this behaviour is consistent with the CERS measurement.

The probe depth is expected to depend only on refractive index and should remain as a constant fraction of the droplet size, $\sim$25% of the droplet radius for ethanol–water droplets.[24] In this work, the probe depth is found to remain a constant fraction of the size that is considerably less than what is expected based on the penetration depth of the WGM. The optical signal is non-linear in nature and follows an exponential dependence on light intensity, leading to a narrower probe depth than WGM penetration depth. Further, this must be also coupled with the enhanced localisation of the signal due to the double resonance nature of the probe, with signal at highest gain arising from the volume of overlap between an input WGM, one resonant with the laser wavelength, and an output mode, one resonant with the Raman band contour. These effects acting in combination lead to greater spatial confinement in the signal when compared with the WGM penetration depth, consistent with previous discussions.[42]

At longer times, the numerical simulations and experimental trends agree that the concentration of the alcohol in the outer

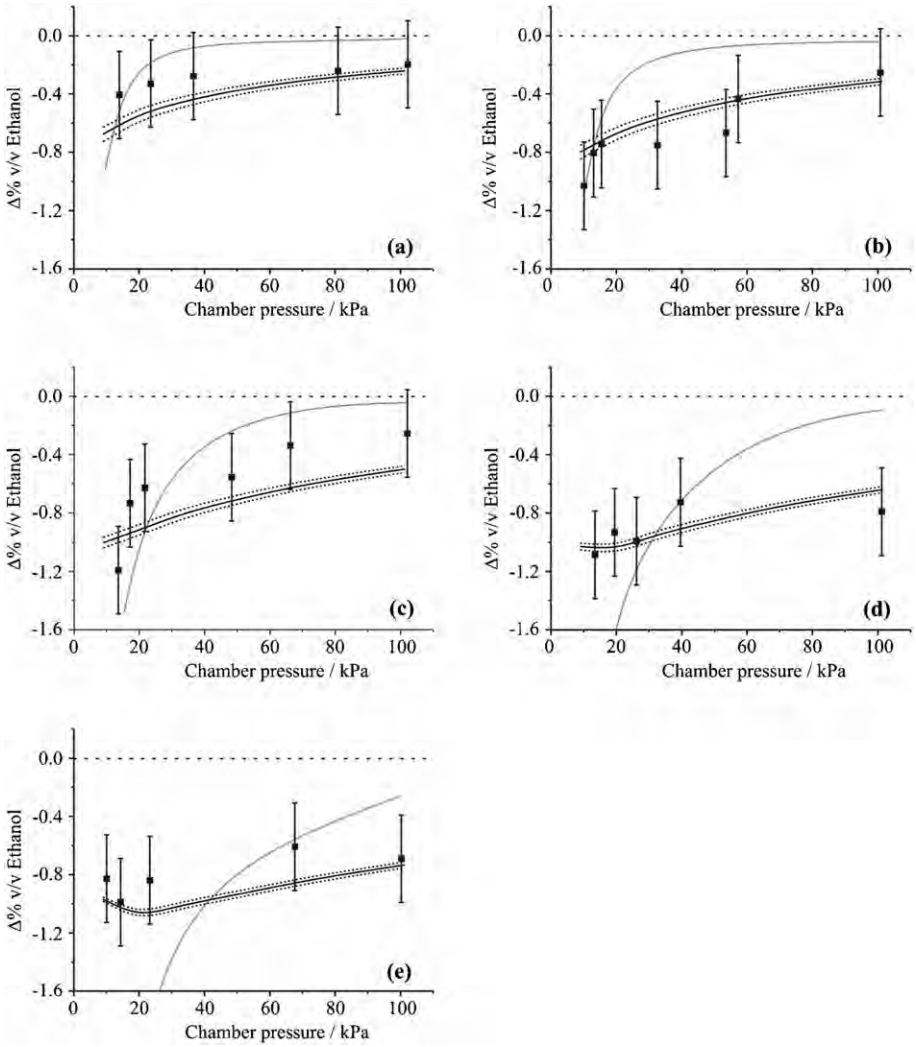

Fig. 8 Pressure dependent evaporation curves which show the ethanol depletion from a 45.3 μm radius droplet at evaporation times of: (a) 0.5 ms, (b) 0.6 ms, (c) 1.3 ms, (d) 2.1 ms and (e) 3 ms. The solid black line represents the numerical simulation for a probe depth of 1400 nm and the black dashed lines represent probe depths of 1300 and 1500 nm. The solid grey line represents predictions from the QSS model.

shell of the droplet recovers. This arises from the enhancement in the diffusional rate of alcohol to the droplet surface from the bulk liquid, leading to the beginning of a recovery of the surface concentration of the alcohol. To our knowledge, this represents the first direct *in situ* measurement of the effect of a concentration gradient on the evaporation of multicomponent droplets and the time-dependent change in the near surface composition of an evaporating droplet.

Appendix A

The thermodynamic description for calculating the equilibrium composition of the vapour above the droplet surface requires knowledge of the variation in the excess Gibbs energy, G^E, with the liquid–phase mixture composition. For this, one has to know the values of parameters of corresponding G^E-equations used for calculation of activity coefficients of the mixture components. Generally, these parameters can be estimated from fits to equilibrium data. In this publication, the activity coefficients for water and ethanol are calculated from the non-random two-liquid (NRTL) model, which is based on a local mole fraction concept developed by Renon and Prausnitz.[43] The activity coefficients are expressed as

$$\ln \gamma_1 = x_2^2 \left[\tau_{21} \left(\frac{G_{21}}{x_1 + x_2 G_{21}} \right)^2 + \frac{\tau_{12} G_{12}}{(x_2 + x_1 G_{12})^2} \right] \quad \text{(A1)}$$

$$\ln \gamma_2 = x_1^2 \left[\tau_{12} \left(\frac{G_{12}}{x_2 + x_1 G_{12}} \right)^2 + \frac{\tau_{21} G_{21}}{(x_1 + x_2 G_{21})^2} \right] \quad \text{(A2)}$$

where x_1 and x_2 are mole fractions of ethanol and water, respectively, and

$$\tau_{12} = \frac{g_{12} - g_{22}}{RT} \quad \text{(A3)}$$

$$\tau_{21} = \frac{g_{21} - g_{11}}{RT} \quad \text{(A4)}$$

$$\ln G_{21} = -\alpha_{12} \tau_{21} \quad \text{(A5)}$$

$$\ln G_{12} = -\alpha_{12} \tau_{12} \quad \text{(A6)}$$

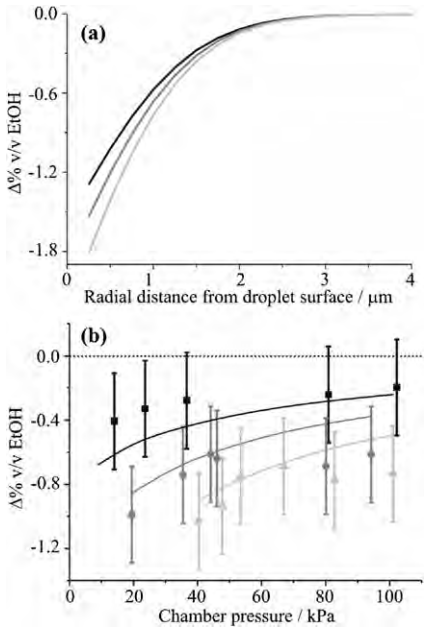

Fig. 9 (a) The change in the ethanol depletion throughout a 45.3 μm radius droplet probed at a fall time of 0.47 ms and at a total chamber pressure of 10 kPa with a partial pressure of water of: 0 kPa, dry nitrogen (black line), 0.523 kPa (grey line) and 1.07 kPa (light grey line). (b) The pressure dependent evaporation curves showing simulated and experimental data obtained from a 45.3 μm radius droplet at a fall time of 0.47 ms. The symbols correspond to experimental measurements and the solid lines to numerical simulations using a probe depth of 1400 nm. The colours of the lines and symbols correspond to the same conditions as in part (a).

Thus, there are three temperature-dependent binary parameters ($g_{12} - g_{22}$, $g_{21} - g_{11}$ and α_{12}) which must be parameterised to fully define the activity coefficients. These parameters are optimized by fitting experimental vapour-liquid equilibrium data from the literature,[44–46] arriving at the following equations:

$$(g_{12} - g_{22})/R = -0.68681T + 261.77 \quad \text{(A7)}$$

$$(g_{21} - g_{11})/R = -8.0894 \times 10^{-5}T^4 + 0.10998T^3 - 56.011T^2 + 1.2667 \times 10^4 T - 1.0729 \times 10^6 \quad \text{(A8)}$$

The solubility of air or nitrogen in the droplets is neglected.

The physical properties for ethanol, water, nitrogen, and air, such as density (ρ), heat capacity (C_P), viscosities (η), surface tension (σ), vapor pressure (P^V), diffusion coefficient for both vapor and liquid,[47] thermal conductivity (K), and enthalpy of evaporation, ΔH_{evp}, are correlated by polynomial regression of literature data[48] and detailed before.[26] The density of the ethanol–water solution is calculated as a function of temperature and ethanol weight fraction, w,

$$\rho = A_0(T - 273.15)^2 + A_1(T - 273.15) + A_2 \quad \text{(A9)}$$

where

$$A_0 = -5.9820 \times 10^{-7}w^2 + 8.8495 \times 10^{-5}w - 3.7194 \times 10^{-3} \quad \text{(A10)}$$

$$A_1 = 1.2845 \times 10^{-4}w^2 - 2.0625 \times 10^{-2}w - 4.4985 \times 10^{-2} \quad \text{(A11)}$$

$$A_2 = -1.05171 \times 10^{-2}w^2 - 0.886516w + 999.748 \quad \text{(A12)}$$

The thermal conductivity of the gas mixtures at low-pressure is calculated by the Lindsay–Bromley method.[49] The thermal conductivity of ethanol solution is given as

$$k = 2.7693x_1^2 - 4.7017x_1 + 1.7054 + (-170.49x_1^2 + 353.93x_1 + 67.064)T \quad \text{(A13)}$$

The heat capacity of the ethanol–water droplet is described as

$$C_P = C_{Pm}^E + x_1C_{P1}^L + x_2C_{P2}^L \quad \text{(A14)}$$

The excess heat capacity (C_{Pm}^E) is given in literature and C_{P1}^L and C_{P2}^L are the molar heat capacity for liquid ethanol and liquid water.[50]

Fuller–Schettler–Giddings theory[47] is used to predict the diffusion coefficients for the vapour phase components. The Vignes relation is used to determine the binary diffusion coefficients at finite concentrations,[51]

$$D_{12} = (D_{12}^0)^{x2}(D_{21}^0)^{x1}\alpha \quad \text{(A15)}$$

where D_{12}^0 and D_{21}^0 are the infinite diffusion coefficients ($m^2\ s^{-1}$) described by the equations[48,52]

$$D_{12}^0 = 1 \times 10^{-9}\exp\left(\frac{-2261.5}{T} + 7.7695\right) \quad \text{(A16)}$$

$$D_{21}^0 = 1 \times 10^{-9}\exp\left(\frac{-2271.9}{T} + 7.7897\right) \quad \text{(A17)}$$

and α can be derived from the NRTL equation as

$$\alpha = 1 - 2x_1x_2\left[\frac{\tau_{21}G_{21}^2}{(x_1 + x_2G_{21})^3} + \frac{\tau_{12}G_{12}^2}{(x_2 + x_1G_{12})^3}\right] \quad \text{(A18)}$$

Acknowledgements

CJH acknowledges the NERC for studentship funding to support this project. JPR acknowledges the EPSRC for financial support for this research and for Advanced Research Fellowship funding for JPR. CJB acknowledges NSF NIRT Grant EEC-0210835, the Air Force Office of Scientific Research Award F49620-01-0168, the DOD MURI Program Contract 318651, and the DOE Basic Energy Sciences Program NSET Grant DE-FG03-02ER15368 for the financial supports.

References

1 R. Vehring, W. R. Foss and D. Lechuga-Ballesteros, *J. Aerosol Sci.*, 2007, **38**(7), 728.
2 G. Gogos, S. Soh and D. N. Pope, *Int. J. Heat Mass Transfer*, 2003, **46**, 283.
3 H. M. Mansour and A. J. Hickey, *AAPS PharmSciTech*, 2007, **8**(4), 140.
4 S. S. Sazhin, *Prog. Energy Combust. Sci.*, 2006, **32**(2), 162.
5 N. Tsapis, E. R. Dufresne, S. S. Sinha, C. S. Riera, J. W. Hutchinson, L. Mahadevan and D. A. Weitz, *Phys. Rev. Lett.*, 2005, **94**(1), 018302.

6 V. Devarakonda and A. K. Ray, *J. Colloid Interface Sci.*, 2000, **221**, 104.
7 G. Castanet, A. Delconte, F. Lemoine, L. Mees and G. Grehan, *Exp. Fluids*, 2005, **39**(2), 431.
8 G. Castanet, M. Lebouche and F. Lemoine, *Int. J. Heat Mass Transfer*, 2005, **48**(16), 3261.
9 A. K. Ray and S. Venkatraman, *AIChE J.*, 1995, **41**(4), 938.
10 J. F. Widmann and E. J. Davis, *Aerosol Sci. Technol.*, 1997, **27**(2), 243.
11 A. K. Ray, E. J. Davis and P. Ravindran, *J. Chem. Phys.*, 1979, **71**(2), 582.
12 E. J. Davis and A. K. Ray, *J. Chem. Phys.*, 1977, **67**(2), 414.
13 E. J. Davis, *Aerosol Sci. Technol.*, 1997, **26**(3), 212.
14 V. Devarakonda and A. K. Ray, *J. Aerosol Sci.*, 2003, **34**(7), 837.
15 R. J. Hopkins and J. P. Reid, *J. Phys. Chem. A*, 2005, **109**, 7923.
16 R. J. Hopkins and J. P. Reid, *J. Phys. Chem. B*, 2006, **110**, 3239.
17 G. Schweiger, *J. Aerosol Sci.*, 1990, **21**(4), 483.
18 R. Vehring, H. Moritz, D. Niekamp, G. Schweiger and P. Heinrich, *Appl. Spectrosc.*, 1995, **49**(9), 1215.
19 F. R. Newbold and N. R. Amundson, *AIChE J.*, 1973, **19**(1), 22.
20 T. Vesala, M. Kulmala, R. Rudolf, A. Vrtala and P. E. Wagner, *J. Aerosol Sci.*, 1997, **28**(4), 565.
21 J. Smolik and J. Vitovec, *J. Aerosol Sci.*, 1984, **15**(5), 545.
22 C. R. Howle, C. J. Homer, R. J. Hopkins and J. P. Reid, *Phys. Chem. Chem. Phys.*, 2007, **9**, 5344.
23 R. J. Hopkins, C. R. Howle and J. P. Reid, *Phys. Chem. Chem. Phys.*, 2006, **8**, 2879.
24 R. Symes, R. M. Sayer and J. P. Reid, *Phys. Chem. Chem. Phys.*, 2004, **6**, 474.
25 *Handbook of Chemistry and Physics*, CRC Press LLC, 2006–2007.
26 X. Jiang, Doctoral Thesis, The University of New Mexico, 2006.
27 J. Ockendon and W. Hodgkins, *Moving Boundary Problems in Heat Flow and Diffusion*, Oxford University Press, Oxford, 1975.
28 R. S. Gupta and D. Kumar, *Comput. Methods Appl. Mech. Eng.*, 1981, **29**(2), 233.
29 R. S. Gupta and D. Kumar, *Int. J. Heat Mass Transfer*, 1983, **26**(2), 313.
30 R. S. Gupta and A. Kumar, *Comput. Methods Appl. Mech. Eng.*, 1984, **44**(1), 91.
31 E. A. Moyano and A. F. Scarpettini, *Num. Methods Partial Differential Equations*, 2000, **16**(1), 42.
32 Rizwan-uddin, *Num. Heat Transfer Part B*, 1998, **33**(3), 269.
33 N. S. Asaithambi, *Appl. Math. Comput.*, 1997, **81**(2–3), 189.
34 J. Caldwell, S. Savovic and Y. Y. Kwan, *J. Heat Transfer*, 2003, **125**(3), 523.
35 H. J. E. Dobson, *J. Chem. Soc.*, 1925, **127**, 2866.
36 X. Qu, E. J. Davis and B. D. Swanson, *J. Aerosol Sci.*, 2001, **32**(11), 1315.
37 G. Chen, M. M. Mazumder, R. K. Chang, J. C. Swindal and W. P. Acker, *Prog. Energy Combust. Sci.*, 1996, **22**(2), 163.
38 R. M. Sayer, R. D. B. Gatherer and J. P. Reid, *Phys. Chem. Chem. Phys.*, 2003, **5**(17), 3740.
39 R. N. Berglund and B. Y. H. Liu, *Environ. Sci. Technol.*, 1973, **7**, 147.
40 R. J. Hopkins, R. Symes, R. M. Sayer and J. P. Reid, *Chem. Phys. Lett.*, 2003, **380**, 665.
41 S. C. Hill and R. E. Benner, *Morphology-Dependent Resonances*, ed. World Scientific, Singapore, 1998.
42 J. X. Zhang and P. M. Aker, *J. Chem. Phys.*, 1993, **99**(12), 9366.
43 H. Renon and J. M. Prausnitz, *AIChE J.*, 1968, **14**, 135.
44 K. Kurihara, T. Minoura, K. Takeda and K. Kojima, *J. Chem. Eng. Data*, 1995, **40**(3), 679.
45 K. Kurihara, M. Nakamichi and K. Kojima, *J. Chem. Eng. Data*, 1993, **38**(3), 446.
46 R. C. Pemberton and C. J. Mash, *J. Chem. Thermodyn.*, 1978, **10**(9), 867.
47 E. N. Fuller, P. D. Schettler and J. C. Giddings, *Ind. Eng. Chem.*, 1966, **58**, 19.
48 *Perry's Chemical Engineers' Handbook*, ed. R. H. Perry, D. W. Green and J. O. Maloney, McGraw-Hill, New York, 1997.
49 A. L. Lindsay and L. A. Bromley, *Ind. Eng. Chem.*, 1950, **42**, 1508.
50 G. C. Benson and P. J. D'Arcy, *J. Chem. Eng. Data*, 1982, **27**, 439.
51 A. Vignes, *Ind. Eng. Chem. Fundam.*, 1966, **5**, 189.
52 K. C. Pratt and W. A. Wakeham, *Proc. R. Soc. London, Ser. A*, 1974, **336**, 393.